



A new parameterization of photolysis rates for oxygenated volatile organic compounds (OVOCs)

Yuwen Peng¹, Bin Yuan¹, Sihang Wang¹, Xin Song¹, Zhe Peng¹, Wenjie Wang², Suxia Yang¹, Jipeng Qi¹, Xianjun He¹, Yibo Huangfu¹, Xiao-Bing Li¹, and Min Shao¹

¹College of Environment and Climate, Institute for Environmental and Climate Research, Guangdong-Hongkong-Macau Joint Laboratory of Collaborative Innovation for Environmental Quality, Jinan University, Guangzhou 511443, China

²Multiphase Chemistry Department, Max Planck Institute for Chemistry, Mainz 55128, Germany

Correspondence: Bin Yuan (byuan@jnu.edu.cn) and Min Shao (mshao@pku.edu.cn)

Received: 7 April 2025 – Discussion started: 15 April 2025

Revised: 12 June 2025 – Accepted: 27 June 2025 – Published: 10 July 2025

Abstract. Oxygenated volatile organic compounds (OVOCs) play a crucial role in atmospheric chemistry, significantly influencing radical production and VOC degradation through photolysis. However, current research on OVOC photolysis is limited by insufficient species coverage in the mechanisms and incomplete understanding from a species-specific perspective. In this study, the photolysis frequencies of 109 OVOCs were compiled into a comprehensive photolysis dataset. Based on their molecular structures, a parameterization for the photolysis frequencies of carbon- and nitrogen-containing OVOCs was developed. By establishing a relationship between species structure and photolysis frequency, this approach avoids the limitation of insufficient quantum yield data, enabling the estimation of photolysis rate constants for compounds lacking experimental measurements. Photolysis frequencies for the dataset species were successfully reproduced with 21 reference values and 10 adjustment coefficients. Using an automated program based on this method, photolysis rate constants for 3039 OVOCs were predicted, and the Master Chemical Mechanism (MCM) v3.3.1 chemical mechanism was updated and expanded to include photolysis for 714 additional species. The introduction of the new photolysis mechanism has altered both the concentrations of photodegradable OVOCs and the relative proportions of their removal pathways. Non-HCHO OVOCs, particularly multifunctional species with carbonyl groups, contribute significantly to RO_x radical production. At three different sites, non-HCHO OVOC photolysis accounts for 25%–45% of RO_x production, surpassing HCHO photolysis. The importance of oxidation products from aromatics and alkenes is highlighted, offering new insights into OVOC photolysis from a species-specific perspective.

1 Introduction

Oxygenated volatile organic compounds (OVOCs) are a subset of VOCs and encompass a range of compounds, including aldehydes, ketones, alcohols, acids, ethers, esters, and highly reactive species such as enals and enones. They significantly affect atmospheric chemistry and contribute to the formation of secondary pollution (Mellouki et al., 2015; Huang et al., 2020). OVOCs originated not only from the oxidation of hydrocarbons but also from primary emissions (McDonald et al., 2018). OVOCs are characterized by their diverse species,

high reactivity, complex sources, and measurement difficulty. With the advancement of modern mass spectrometry technologies, the importance of OVOCs is gradually being revealed, contributing 16%–51% to the total concentrations of VOCs in different environments (Liu et al., 2020; Li et al., 2020; Hui et al., 2018; Jing et al., 2020; Song et al., 2023). OVOCs are removed from the atmosphere through reactions with oxidants, wet or dry deposition, and photolysis (Mellouki et al., 2015). The photolysis rate influences the relative importance of removal pathways for photodegradable OVOCs. For some species, photolysis serves as the dominant

sink and governs their atmospheric fates (Yuan et al., 2016; Eger et al., 2020).

Through photolysis, OVOCs can produce atmospheric radicals such as RO_2 and HO_2 , which enhance atmospheric oxidation capacity and contribute to ozone formation (Tan et al., 2019a, b; Kanaya et al., 2007; Griffith et al., 2016). The photolysis of OVOCs plays a significant role in the production of RO_x radicals ($\text{RO}_x = \text{RO}_2 + \text{HO}_2 + \text{OH}$) (see Fig. 1 and Table S1 in the Supplement) and can account for over 80 % of the production of RO_x ($p(\text{RO}_x)$) during the later stages of winter ozone pollution (Edwards et al., 2014). OVOCs from different sources play varying roles in their contributions to atmospheric oxidation capacity. Primarily emitted OVOCs act as primary radical producers, capable of directly generating 1 to 2 radicals through photolysis, resulting in a net production of radicals. This net production provides a substantial supply of radicals for the initial oxidation processes in atmospheric chemistry (Mellouki et al., 2015). At the same time, OVOCs formed through secondary processes serve as “photochemical amplifiers” accelerating the formation of secondary pollutants. OVOCs produced from oxidation may undergo photolysis to produce additional radicals, further contributing to the formation of more OVOCs (Qu et al., 2021). This creates a positive feedback loop that has been recognized as a key factor in high winter ozone concentrations in multiple regions (Edwards et al., 2014; Li et al., 2021). Furthermore, as primary radical producers, OVOC photolysis increases the production of RO_x , while as photochemical amplifiers, they increase radical chain length. Thus, the photolysis of OVOCs effectively enhances atmospheric oxidation capacity.

However, several challenges remain that hinder our ability to better constrain the environmental effects of OVOC photolysis. Firstly, current chemical mechanisms fail to fully account for recently reported photodegradable species, such as some multifunctional compounds (Newland et al., 2019; Tomas et al., 2021; Müller et al., 2014; Wang et al., 2023). Traditional mechanisms mainly focus on mono- or bi-functional, low-carbon species (see Sect. S1 and Fig. S9 in the Supplement). Secondly, significant discrepancies exist in the reported photolysis frequencies of certain species (e.g., nitrophenol or benzaldehyde; Peng et al., 2023; Mellouki et al., 2015). These differences largely arise from varying estimates of quantum yield, which can lead to differences in photolysis rate constants by nearly an order of magnitude. Furthermore, many species remain unmeasured or lack sufficient reporting. Although the development of modern measurement techniques has greatly expanded the range of measurable species (Ye et al., 2021; Yuan et al., 2017), it is still prohibitively expensive in terms of time and cost to measure photodegradable species individually. Currently, the MPI-Mainz UV/VIS database includes absorption cross-section data for 310 organic compounds, but quantum yield information is only available for formaldehyde and acetaldehyde (Keller-Rudek et al., 2013). Similarly, the IUPAC database

provides absorption cross-sections and photolysis product data for 39 compounds, yet more than half of these species lack recommended quantum yield values or assume a quantum yield of 1 across all wavelengths (IUPAC, 2012). The scarcity and uncertainty of quantum yield data remain significant limitations in deriving accurate photolysis rate constants for OVOCs. Finally, due to the incomplete description of mechanisms, current evaluations for the contribution of OVOC photolysis to atmospheric oxidation capacity primarily focus on simple species such as formaldehyde (Tan et al., 2019a; Young et al., 2012) or treat OVOCs as a whole (Liu et al., 2012; Yang et al., 2018).

Several parameterization approaches for OVOC photolysis rate constants have been developed, including Master Chemical Mechanism (MCM) (Jenkin et al., 1997, 2003), the Generator for Explicit Chemistry and Kinetics of Organics in the Atmosphere (GECKO-A) (Aumont et al., 2005), and the SAPRC mechanism generation system (MechGen) (Carter et al., 2025). MCM v3.3.1 applies a core set of 20 reactions parameterized as functions of the solar zenith angle, with surrogate parameters for species with limited data, but sometimes assigns identical rates to structurally distinct compounds. GECKO-A focuses on three primary chromophores (carbonyls, hydroperoxides, nitrates) and employs detailed cross-section datasets for 54 species, yet it lacks differentiation among conjugated systems or less common photodegradable functional groups. MechGen, developed specifically for the SAPRC mechanism, assigns overall quantum yields to representative species based on grouped reactivity. However, it assumes that quantum yields are wavelength-independent and provides only lumped quantum yields rather than explicit photolysis rate constants. Consequently, there is no comprehensive or easily accessible source for photolysis rate constants of a specific OVOC species, as the existing data are dispersed across various studies. These limitations highlight the need for a structure-specific approach that directly outputs the photolysis rate constant and captures a wide range of functional group combinations.

In this study, we have integrated the most recently reported photolysis frequency data to obtain a dataset of OVOC photolysis. From this dataset, we establish a relationship between the chemical structures of OVOCs and their photolysis rate constants, avoiding the need for inaccessible quantum yield data across many species. Based on this dataset, a new parameterization method was proposed to predict photolysis frequencies based on molecular structures. Subsequently, these predicted photolysis frequencies were incorporated into chemical mechanisms and were evaluated using an observation-based box model to quantitatively assess the atmospheric impacts.

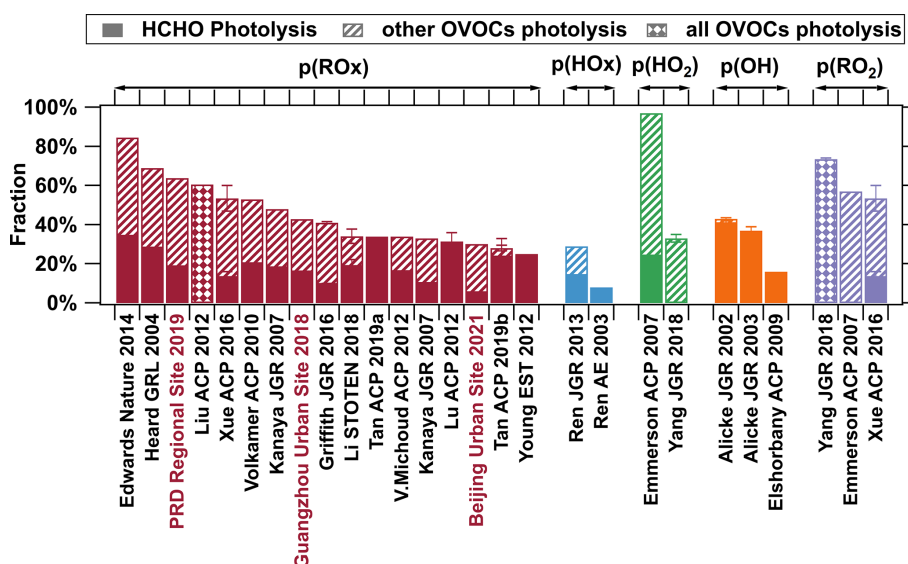


Figure 1. Contributions of OVOC photolysis to the production rates of radicals in different environments. RO_x represents the sum of HO₂, RO₂, and OH, while HO_x is the sum of HO₂ and OH. The contributions of OVOC photolysis at the three sites determined in this study are shown in red. Detailed data, locations, season and year of the measurements, and references are provided in Table S1.

2 Method

2.1 Observation

Field measurements were conducted at three sites, representing both urban and regional environments in southern and northern China. The urban site in southern China was located at the Guangzhou Institute of Geochemistry (GIG), Chinese Academy of Sciences (23.1°N, 113.2°E), in the urban area of Guangzhou. Instruments were deployed approximately 25 m above ground level, and measurements were taken during the fall of 2018 (September to November). The site was surrounded by residential areas and roadways (Wu et al., 2020; Wang et al., 2020; Yang et al., 2022). The urban site in northern China was in downtown Beijing, where a 3-month field campaign was conducted from May to August of 2021. The site was located at the Institute of Atmospheric Physics (IAP), Chinese Academy of Sciences (23.15°N, 113.36°E), which is a large meteorological and environmental monitoring tower in the bustling city center (Li et al., 2025; Huangfu et al., 2024). Data collected from 7 to 31 July at an approximate height of 5 m above the ground were used in this study. The regional site was the Guangdong Atmospheric Supersite (22.7°N, 112.9°E) situated in Heshan (HS), approximately 80 km southwest of Guangzhou and frequently influenced by anthropogenic emissions from the Guangzhou–Foshan megacity. Observations were conducted during the fall of 2019 (October–November), characterizing it as a representative regional receptor site in the Pearl River Delta (PRD) (Cai et al., 2024; Yang et al., 2022).

OVOCs were measured at all three sites using a high-resolution proton-transfer-reaction quadrupole-interface

time-of-flight mass spectrometer (PTR-QiToF-MS, ION-ICON Analytik, Austria) (Wu et al., 2020; He et al., 2022). At the Guangzhou urban site and PRD regional site, non-methane hydrocarbons (NMHCs) were measured hourly using a gas chromatograph equipped with a flame ionization detector and a mass spectrometer (GC-MS-FID, Wuhan Tianhong Co., Ltd, China) (Wang et al., 2022). NMHCs data from the Beijing urban site were unavailable, so we estimated those unmeasured species according to proton-transfer-reaction time-of-flight mass spectrometer (PTR-ToF-MS) data, data from nearby stations, and OH reaction rate constants (k_{OH}) of individual species with OH radicals. Detailed estimation methods are provided in the “Supporting Information” of Li et al. (2025).

Details regarding the measurement of meteorological parameters, photolysis rates, and trace gases at the three sites, including instruments used and specific measurement methods, are provided in Sect. S2. Further details on the instruments used at each site are provided in Wang et al. (2022) for the Guangzhou urban site, Yang et al. (2024) for the Beijing urban site, and Yang et al. (2022) for the PRD regional site. Temporal variations in typical photodegradable species at each site, along with reference parameters including O_x, NO_x, O₃, temperature, relative humidity, and j_{NO_2} , are presented in Fig. S1.

2.2 Box model description

A zero-dimensional box model, built on the Framework for 0-D Atmospheric Modeling (F0AM) v4.3 (Wolfe et al., 2016), was applied in this study to compare mechanisms and evaluate their atmospheric impacts. The chemical mech-

anisms included the MCM v3.3.1 (Jenkin et al., 2015; Bloss et al., 2005; Jenkin et al., 2003) and the photolysis mechanism proposed in this study. MCM has been widely used for modeling atmospheric radicals and secondary products (Aumont et al., 2005; Edwards et al., 2014; Chen et al., 2022). The model was constrained using 5 min averaged relative humidity, ambient temperature, pressure, photolysis frequencies, and concentrations of directly measured trace gases and VOCs (listed in Table S2). Simulations were performed until steady-state conditions with a 3 d spin-up period to allow for the buildup of unmeasured intermediate species (Yang et al., 2022). To prevent the unrealistic accumulation of long-lived species, an empirically derived first-order physical dilution coefficient k_{dil} was applied, with values of $1.2 \times 10^{-5} \text{ s}^{-1}$ for both urban sites (equivalent to a 24 h lifetime) and $3.5 \times 10^{-5} \text{ s}^{-1}$ for the PRD regional site (equivalent to an 8 h lifetime) (Yang et al., 2022). In addition to the MCM v3.3.1 mechanism, the photolysis reaction of ClNO_2 has been included, the frequency of which is derived by reducing the j_{NO_2} by a factor of 30 (Riedel et al., 2014).

In this study, we designed two model scenarios to explore atmospheric effects of the newly proposed photolysis mechanism and to identify key species that significantly contribute to the production of total radicals. Scenario 1 was designed to investigate the impact of the new photolysis mechanism under traditional simulation settings. Among all the OVOC species, only formaldehyde (HCHO) was constrained to its measured concentrations. This setup allowed us to assess the impacts of the photolysis mechanism on the atmospheric chemical simulations with the common practice, which facilitated comparing our findings with other studies. However, a key limitation of Scenario 1 is that it may not accurately simulate many organic intermediates. The inadequate representation of these intermediates hindered a more detailed analysis of the key species involved in atmospheric chemistry. To address this issue, Scenario 2 was constrained by 20 additional non-HCHO OVOCs (listed in Table S4) based on PTR-ToF-MS measurements and applied with a dynamic allocation method to semi-quantitatively estimate concentrations from PTR-ToF-MS, thereby constraining over 1300 OVOC intermediates. A detailed description of the dynamic allocation method can be found in Sect. S3 and Fig. S10. By incorporating a broader range of OVOC constraints, Scenario 2 allowed for a more accurate representation of atmospheric reactions and provided deeper insights into the role of OVOC photolysis in driving radical production. Aside from the differences in the constraints on OVOC concentrations, both scenarios follow the same setup as described in the previous section.

2.3 Photolysis dataset for parameterization

The photolysis frequencies can be calculated by numerical summation over wavelength using Eq. (1) (Calvert et al.,

2002).

$$J = \int \delta_i \times \phi_i \times F_i d\lambda_i \quad (1)$$

δ_i , ϕ_i , and F_i stand for the absorption cross-section, quantum yield, and spectral actinic flux of the species i , respectively. The absorption cross-section and quantum yield are typically obtained through laboratory measurements, while the actinic flux is usually acquired through field measurements or models.

A dataset for OVOC photolysis rate constants has been constructed for the subsequent development of parameterization. The data within the dataset are collected from databases like MPI-Mainz UV/VIS (Keller-Rudek et al., 2013) and IUPAC (Mellouki et al., 2021), as well as from textbooks (Calvert et al., 2011) and other relevant literature (see the “Species Dataset” sheet in the Supplement for details). The tropospheric ultraviolet and visible (TUV) radiation model (version 5.3) (Madronich and Flocke, 1999; Lantz et al., 1996) was used to provide a spectral actinic flux under clear-sky conditions. Before inclusion into the dataset, all data were converted to the ratio of photolysis frequencies of OVOC species under overhead sun conditions ($j_{\text{OVOC, overhead}}$) to those for the reference species ($j_{\text{NO}_2, \text{overhead}}$), which is referred to as the relative photolysis frequencies $j_{\text{rel}} (= j_{\text{OVOC, overhead}} / j_{\text{NO}_2, \text{overhead}})$. The relative photolysis frequencies can be conveniently applied to different environments by conversion with measured j_{NO_2} . The data inclusion process is depicted in Sect. S4 and Fig. S11.

The photolysis dataset is divided into a reference group and a comparison group. In the current photolysis dataset, the reference group encompasses a total of 195 photolysis rate constant data entries for 109 OVOC species, including 5 pairs of isomers. The comparison group includes 50 data entries covering 38 species from 8 reports. The reference group primarily consists of data from smog chamber measurements and peer-reviewed recommended data, which will be used for the construction of parameterization schemes. The data in the comparison group mainly consist of the results measured at a single wavelength, results obtained by measuring absorption cross-sections but estimating quantum yields, and estimates for entire categories of substances, such as the single value provided by Treves and Rudich (2003) for hydroxy nitrates containing 3 to 6 carbon atoms. Additionally, results from quantum chemical calculations are also included in the comparison group. Since it mainly includes data with larger uncertainties than the reference group, the comparison group is only used for comparison and not for the construction of the parameterization.

For all OVOC species in the dataset, the simplified molecular input line entry system (SMILES) format is used to describe their molecular structures. SMILES is a specification that uses ASCII strings to explicitly describe molecular structures. Not only is it capable of covering all chemical formulas, but it is also highly readable, is easy to understand,

and has been adopted by many leading international chemical databases (Weininger, 1988; Wang et al., 2018).

3 Results and discussion

3.1 Development of a structural-based parameterization method

An analysis of the relationship between the relative photolysis rate constant (j_{rel}) and species characteristics revealed no significant correlation between j_{rel} and the number of oxygen atoms in the molecules. However, some aromatics, nitrates, aldehydes, and hydroxy carbonyls show a slight increase in j_{rel} with rising carbon oxidation states (OS_{C}), calculated following the method of Kroll et al. (2011), while other species display no significant trends. Interestingly, j_{rel} tend to increase with the number of functional groups in the molecules, except for N-nitrosamines and alkyl nitrites (Fig. S2). Although no clear correlation was observed between j_{rel} and the number of carbon atoms, compounds with similar functional groups tend to cluster within a specific range of j_{rel} (Fig. 2). When j_{rel} of the species in the same compound class are averaged, distinct differences emerge between functional group types, suggesting that the parameterization should focus on the types and quantities of functional groups present in the species.

The photolysis data for OVOCs collected from multiple literature sources were classified based on their functional groups. Compounds within the same family, particularly those with similar functional groups, generally exhibit analogous absorption cross-sections in the UV–visible spectrum (see Fig. S3). This property serves as an essential theoretical basis for structure-based estimation. During oxidation processes, when new functional groups are added to existing molecular structures, conjugation may occur between different chromophores. Such an interaction cannot be simply treated as the additive effects of two individual chromophores, making it necessary to discuss different conjugated systems categorically.

A comparison of data from different literature sources revealed consistent photolysis rate constants for most species, with notable differences observed for certain compounds, such as benzaldehyde, pyruvic acid, peracetic acid, and 2-butenedial (Fig. S4). Based on the 195 entries in the OVOC photolysis dataset, the reported values for the same compound from different literature sources were first averaged, obtaining the averaged data for 109 OVOCs (“Averaged Dataset” sheet in the Supplement). The averaged j_{rel} for 109 compounds were then classified into 23 categories according to their functional group types. These j_{rel} form a dataset for the development of a more accurate parameterization.

Based on the summarized photolysis frequencies, the reference values for 21 classes of compounds were calculated to provide guidance for predicting the photolysis frequencies of the compounds in the same classes containing more

carbon atoms. Taking the example of *n*-aldehydes, one of the most extensively studied groups, their absorption band appears in the ultraviolet B (UVB) region (around 280 nm) due to a weak $n \rightarrow \pi^*$ electronic transition, overlapping partially with the tropospheric radiation spectrum (> 290 nm) (Calvert et al., 2011). The absorption cross-sections of *n*-aldehydes containing 1 to 7 carbon atoms are shown in Fig. S11. For formaldehyde (HCHO), the carbonyl carbon is attached with two hydrogen atoms, and the stretching vibration of the C=O double bond in the π^* excited state is particularly prominent in the absorption band, resulting in significant fluctuations in its absorption cross-section. As the carbon chain length increases, the stretching vibration of the C=O bond in the π^* excited state becomes less pronounced, and the absorption bands nearly overlap (Calvert et al., 2011). Although the absorption of *n*-heptanal (*n*-C₆H₁₃CHO) is slightly higher than that of *n*-pentanal, it is reasonable to consider that, for *n*-aldehydes, the absorption cross-sections and photolysis rate constants become similar once the carbon number reaches 3 or higher. This assumption is consistent with a previous study (Tadić et al., 2001). Therefore, in calculating the reference photolysis rate constants for the aldehyde carbonyl group (-CHO), the average photolysis rate constants of aldehydes with 3 to 7 carbons are used as the reference value ($0.18 \pm 0.053\%$ j_{NO_2}) for aldehydes with 8 or more carbons. In addition to *n*-aldehydes, photolysis reference values were calculated for other 20 classes of species, including substituted aldehydes (e.g., nitrobenzaldehydes, aromatic aldehydes, unsaturated aldehydes, and dialdehydes), nitrogen-containing compounds (e.g., N-nitrosamines, nitrophenols, nitroaromatics, alkyl nitrites, carbonyl nitrates, and peroxy nitrates), ketones (e.g., diketones, cyclic ketones, and unsaturated ketones), and other species such as dienedials, keto acids, hydroperoxides, and peroxy acids (see Fig. 3). The reference values for corresponding species with 1 to 20 carbons are tabulated for clarity (see the “Reference Value Table” sheet in the Supplement). By establishing a relationship between the photolysis rate constants and carbon number, the reference photolysis rate constants for higher-carbon compounds are estimated. The calculation methods for these functional groups are similar to those of aldehydes, with details provided in Sect. S5 and Figs. S12–S30. The parameterization is currently applicable only to compounds composed of carbon (C), hydrogen (H), oxygen (O), and nitrogen (N). Functional groups involving sulfur, halogens, or other elements are not involved in this study due to limited availability of data for these compounds. For a similar reason, the current parameterization does not include epoxy compounds or anhydrides either.

In addition to the reference values, adjustment coefficients were introduced to reflect the influence of different molecular structures more accurately on photolysis rate constants. For example, when 2 methyl groups substitute both α -carbons of 3-pentanone (forming 2,4-dimethyl-3-pentanone), the absorption significantly increases, likely due to a redshift

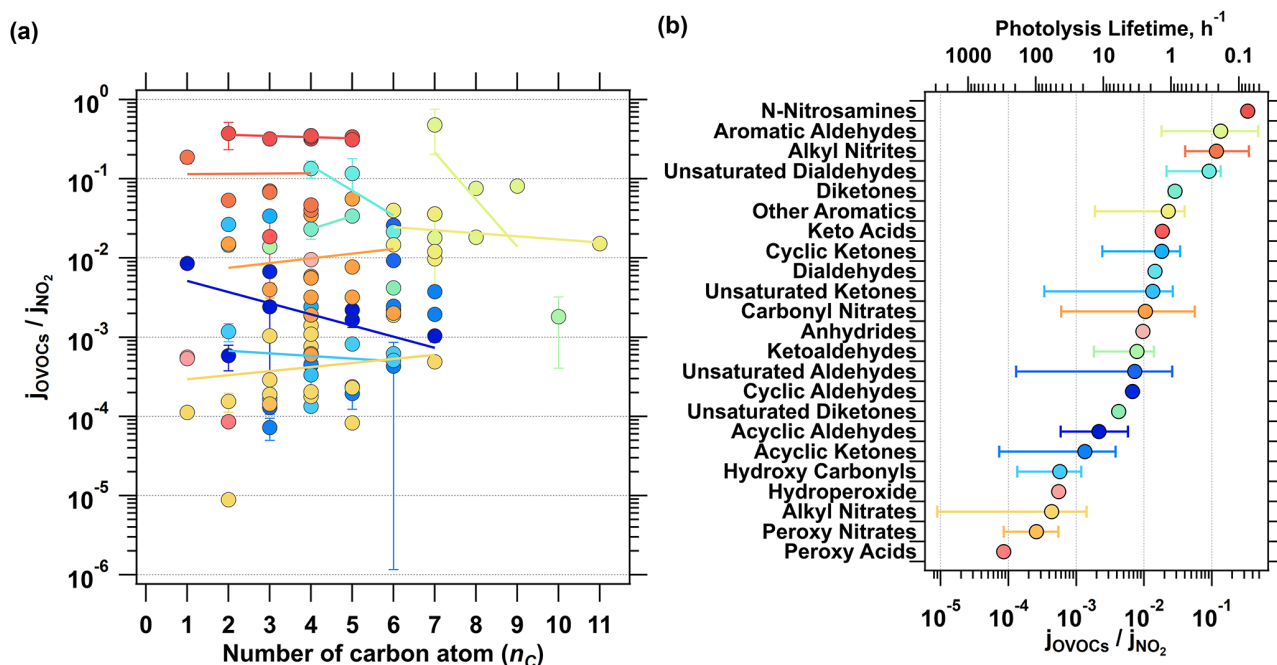


Figure 2. Relationship between the relative photolysis rate constants of OVOCs and the number of carbon atoms (a) and the range of relative photolysis rate constants for different categories of OVOCs after averaging with each class (b). The top axis of panel (b) indicates the corresponding lifetimes against photolysis under overhead sun conditions, based on the j_{rel} , as a reference.

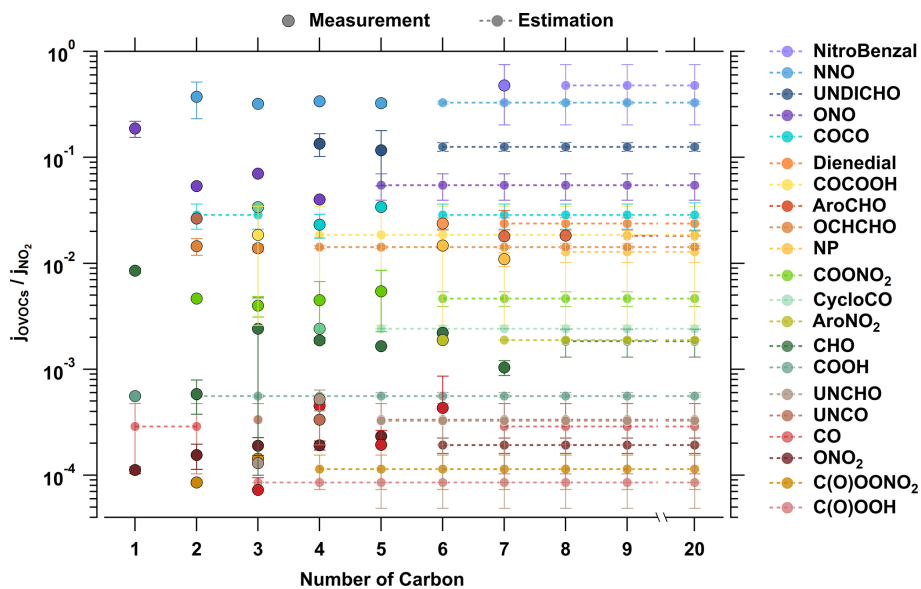


Figure 3. Variation in photolysis reference values of 21 different classes of OVOCs with the numbers of carbons in the molecules. The scatter points in the figure represent measured values from the dataset, while the dashed lines and the points connected by them indicate predicted values for the higher-carbon-containing species.

caused by the inductive effect of alkyl groups, resulting in an enhancement of 0.36 % j_{NO_2} for the photolysis frequencies (due to the lack of photolysis data for 3-pentanone, 2-pentanone is used as a surrogate here). By identifying such relationships and evaluating them against the corresponding

reference values for their respective carbon numbers, a total of 10 adjustment coefficients have been introduced in the current parameterization. The specific basis and calculation process for other parameters can be found in Sect. S6 and Figs. S31–S33. The introduction of adjustment coefficients

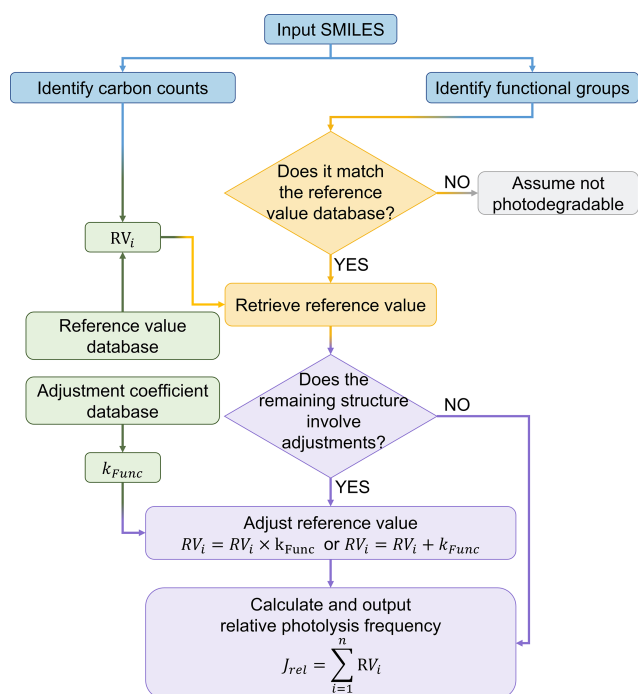


Figure 4. Flowchart of structural-based photolysis frequency parameterization.

enhances the applicability and accuracy of the parameterization for estimating photolysis rate constants of compounds with diverse molecular structures.

Finally, to enable the estimation for a vast number of OVOCs, we developed a program to automate structure recognition and photolysis frequency estimation, as shown in Fig. 4 for the workflow of the program. The program utilizes the SMILES as the input format to identify the carbon count and characterize both the types and quantities of functional groups. Then, the corresponding reference value and adjustment coefficients from the pre-established dataset are retrieved to calculate and output the predicted photolysis frequencies of the OVOC in the form of j_{rel} . This approach effectively reproduces the j_{rel} of 104 compounds from the reference group of the dataset (Fig. 5a). The main deviations arise from underestimations for nitro-naphthalene, 2-acetylbenzaldehyde, and 2-hexenal, as well as overestimation for hydroxy butanone, highlighting areas for future optimization. Compared to the measured data in the dataset, 81 % of the species fall within a $\pm 50\%$ deviation range and 98 % within a factor of 2 (Fig. 5a). The strong agreement between measured and predicted values ($R^2 = 0.92$) indicates the reliable performance of this proposed parameterization method (Fig. 5a).

For the 50 species in the comparison group, the estimated results from this study align well with j_{rel} of approximately half of the species (Fig. S5). Taking nitrocatechols as an example, their j_{rel} were estimated based on those of structurally similar nitrophenols, as both share aromatic rings substituted

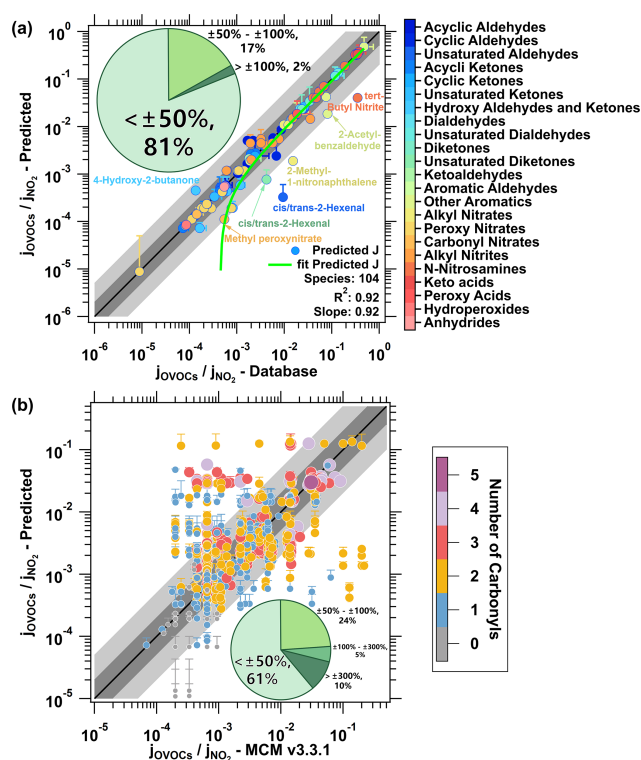


Figure 5. Comparison of predicted j_{rel} in this study and the measured j_{rel} in the reference group (a) or the j_{rel} in the MCM v3.3.1 mechanism (b). Each point corresponds to a specific compound, with species showing larger deviations labeled for clarity. The green curve in panel (a) represents the fitted prediction. Different colors and sizes of the points in panel (b) represent the number of carbonyl groups in each species. The black line indicates the 1 : 1 agreement and the darker gray band represents a deviation of a factor of 2, while the lighter gray band extends to a deviation of a factor of 5. The subplot pie chart illustrates the distribution of the relative deviation, calculated as (predicted – measured)/measured.

with OH and NO₂ groups. The parameterization effectively reproduces the j_{rel} of four types of nitrocatechols measured by Roman et al. (2022) using chamber experiments, further demonstrating the reliable performance of the method. Notable deviations mainly originate from two studies. Wang et al. (2023) reported significantly lower j_{rel} for three classes of monoterpene-derived organic nitrates, while Liu et al. (2018) estimated the j_{rel} of α -hydroperoxycarbonyls to be only about 7 % of our estimated value. These differences can be explained by the substantial uncertainties in the comparison dataset, which was derived from eight independent studies that employed a variety of methodologies, such as quantum chemical calculations, single-wavelength measurements, and indirect estimates based on absorption cross-sections combined with assumed quantum yields. In addition, the current method does not incorporate structure-specific adjustments for certain compound classes, which may also contribute to the observed discrepancies.

3.2 Comparison to Master Chemical Mechanism v3.3.1

As a detailed mechanism, MCM includes 5809 species and intermediates, among which 2327 are classified as photodegradable. Our estimates of j_{rel} align with MCM within $\pm 50\%$ for 61% of the evaluated species (Fig. 5b). Among all the photodegradable species in the MCM, two species (CH₃SOOOH and ETOMENO₃) are identified as non-photodegradable, as the method used is not applicable to sulfur-containing species and ETOMENO₃ lacks photoreactive chromophores. Consequently, no photolysis rate constants were generated for them. The differences in photolysis rate constants primarily arise from differences in the classification and estimation of functional groups for multifunctional compounds (Fig. 5b). The parameterization method produces higher values for species such as aromatic aldehydes, multi-carbonyl compounds, nitrate esters, and hydroxyl nitrate esters, while it yields lower values for species including carbonyl hydroperoxides, unsaturated diketones, hydroxy nitrates, and hydroxycarboxylic acids when compared to MCM. The detailed estimation results for 2327 photodegradable species can be found in the “Prediction-MCM2327” sheet in the Supplement. An updated MCM v3.3.1 mechanism that can be directly used in the FOAM box model is available in the file named “MCMv331_OVOCshv_updated_Mech” on the figshare website (Peng, 2025).

In addition to these 2327 photodegradable species identified in MCM, this study further identifies 714 additional photodegradable species from the 5809 species in MCM based on their structural characteristics. The 714 newly identified species are primarily characterized by their diverse chromophore, including carbonyl groups, nitrates (e.g., ONO₂, C(=O)ONO₂, C(=O)OONO₂), and hydroxyl groups (OH). A notable proportion (38%) of these species contain ring structures, suggesting their origin from aromatic hydrocarbon, terpenes, or other polycyclic compounds. Additionally, 46% of the newly identified species contain two or more chromophores, further emphasizing the need for more comprehensive evaluation of multifunctional species. The photolysis rate constants of these photolysis reactions were determined using the structure-based parameterization, while the reaction products were inferred based on existing patterns of known products, producing 1 to 2 radicals. Details of the newly coupled photolysis module with MCM v3.3.1 are provided in the “714 Newly Add Species” and “Additional OVOCs Mech” sheets in the Supplement. A supplementary mechanism that can be directly used in the FOAM box model is available in the file named “MCMv331_OVOCshv_updated_Mech” on the figshare website (Peng, 2025). Details on surrogate products for unknown photolysis reactions can be found in Sect. S7. The modifications to photolysis reactions, including photolysis rate constants and reaction products, are incorporated

in the standard MCM v3.3.1 as a newly updated chemical mechanism.

The application of the new photolysis mechanism has influenced both the concentration of photodegradable OVOCs and the relative contributions of their removal pathways. Compared to the standard MCM mechanism, a 50% or greater increase in the concentration of OVOCs was observed for 9% of photodegradable species at the Guangzhou urban site, and for 16% at the PRD regional site (Fig. 6a, b). Some species exhibited an increase in concentration even when photolysis was enhanced, which was observed for 9.2% of species at the Guangzhou urban site, and for 11% at the PRD regional site. This observation may be attributed to the positive feedback between the radicals generated by the enhanced photolysis of these OVOCs and the oxidation of their precursors, leading to the formation of additional photodegradable products. This effect is consistent with the findings of Qu et al. (2021), where OVOC photolysis contribute to the amplification of radical cycling in the atmosphere.

The changes in concentrations of OVOCs reflect variations in their atmospheric budget. Here, the ratio of $j_{\text{OVOC}}/(k_{\text{OH}} \times [\text{OH}])$ is used to represent the relative importance of two pathways for each OVOC species: photolysis and reactions with OH radicals (Fig. 6c, d). The ratio is calculated by dividing the photolysis removal rate by the OH reaction removal rate for each species, and the campaign average is then computed to obtain the mean ratio for each species. After adopting the new photolysis scheme, the relative importance of photolysis increased for over half of the photodegradable OVOC species at both sites. For the campaign-averaged $j_{\text{OVOC}}/(k_{\text{OH}} \times [\text{OH}])$, the new mechanism shows a 25% increase (from 1.2 to 1.5) at the Guangzhou urban site and a 21% increase (from 1.7 to 2.1) at the PRD regional site. From the perspective of the number of carbonyl functional group in each species, species containing zero to one carbonyl group are removed from the atmosphere mainly via reaction with OH radicals rather than photolysis. For species containing two or more carbonyls, photolysis dominates their atmospheric removal. The averaged $j_{\text{OVOC}}/(k_{\text{OH}} \times [\text{OH}])$ for compounds with 2 or more carbonyls is 4.4 at the Guangzhou urban site and 6.1 at the PRD regional site, indicating that photolysis is a more important removal pathway than reaction with OH radicals for multi-carbonyl compounds. At the Guangzhou urban site, the new mechanism increased the $j_{\text{OVOC}}/(k_{\text{OH}} \times [\text{OH}])$ value by 34% for species with 0–1 carbonyls and by 188% for species with more than 3 carbonyls, while the ratio decreased by 27% for species with 2 carbonyls. Similar changes were observed at the PRD regional site. This suggests that previous mechanisms may overestimate the photolysis of di-carbonyl compounds while underestimating the photolysis of multi-carbonyl compounds. Late-generation VOC oxidation products, especially those with multiple carbonyl groups, warrant further investigation into their role in photolysis as part of their atmospheric removal pathway.

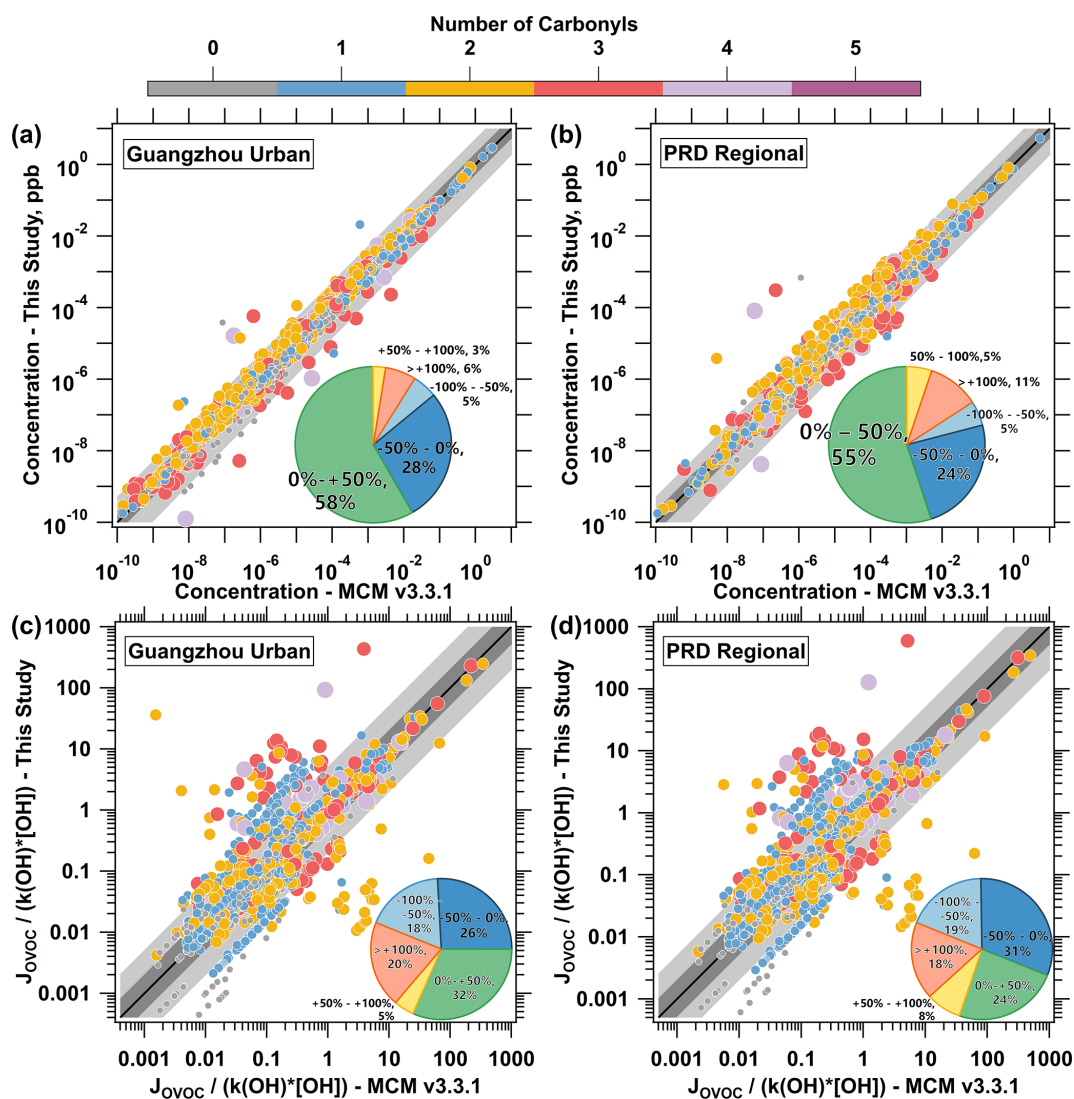


Figure 6. Comparison of concentration of photodegradable species (a, b), and the ratio of $j_{\text{OVOC}}/(k_{\text{OH}} \times [\text{OH}])$ (c, d) in the MCM V3.3.1 mechanism and predictions from this study in Scenario 1. Each point represents a specific compound and sizes of the points represent the number of carbonyl groups in each species. The black line indicates the 1 : 1 agreement, and the darker gray band represents a deviation of a factor of 2, while the lighter gray band extends to a deviation of a factor of 5. The subplot pie chart illustrates the distribution of the relative deviation, calculated as (this study – MCM)/MCM.

The updated mechanism not only influences OVOCs themselves but also affects the production of RO_x radicals in our simulations. A significant contribution from non-HCHO OVOC photolysis to RO_x radical production was observed at both sites, with an enhancement in $p(\text{RO}_x)$ upon application of the updated photolysis mechanism. After implementing the updated mechanism, the averaged daytime contribution of non-HCHO OVOC photolysis to $p(\text{RO}_x)$ increased from 36 % to 40 % at the Guangzhou urban site (Fig. 7, with a detailed comparison of non-HCHO OVOC contribution in Fig. S6). In contrast, the contribution from HCHO photolysis remained relatively low at 13 %. Similarly, at the PRD regional site, the averaged daytime contribution of non-HCHO

OVOC photolysis increased from 44 % to 47 %, which is 2.6 times that of HCHO photolysis (Fig. 7). As a result, the total daytime $p(\text{RO}_x)$ reached 2.9 ppb h^{-1} at the Guangzhou urban site and 3.7 ppb h^{-1} at the PRD regional site. Notably, at noon when RO_x production peaked, $p(\text{RO}_x)$ showed an increase of 7.6 % at the Guangzhou urban site and 8.8 % at the PRD regional site. These findings highlight the dominant role of non-HCHO OVOC photolysis in driving RO_x radical production, surpassing the contribution from formaldehyde photolysis.

Under the influence of the new photolysis mechanism, more than 2000 OVOC species collectively contributed to changes in $p(\text{RO}_x)$ levels. The implementa-

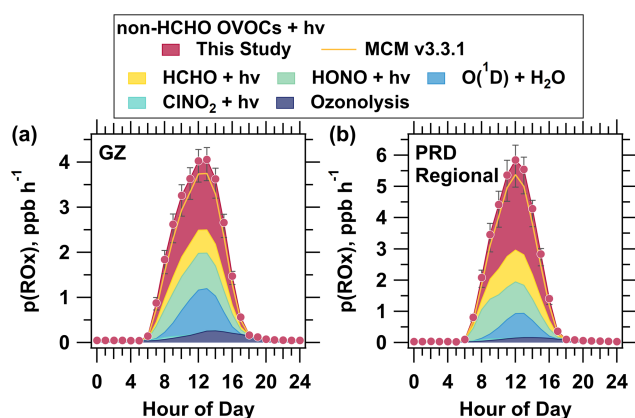


Figure 7. Source composition of total $p(\text{RO}_x)$ at the Guangzhou urban site (a) and PRD regional site (b) under Scenario 1. The yellow solid lines represent the scenarios simulated using the MCM v3.3.1 mechanism, while the shaded areas indicate the contributions of different pathways to $p(\text{RO}_x)$. Error bars (this study only) show the range from using the maximum and minimum estimated photolysis rate constants in the simulations.

tion of this new mechanism led to an increased contribution to $p(\text{RO}_x)$ from non-carbonyl-containing OVOCs (e.g., nitrophenols), unsaturated mono-carbonyl species (e.g., methacrolein, MACR), and saturated tri-carbonyl compounds (e.g., 3,4-dioxopentanal) at both sites (Fig. 8). The greatest absolute increase in $p(\text{RO}_x)$ was observed for unsaturated mono-carbonyl compounds at the PRD regional site, followed by non-carbonyl-containing OVOCs, with mean increases of 2.4 and 1.0 ppb d^{-1} , respectively. In contrast, the contribution of unsaturated di-carbonyl compounds (e.g., 2-methylbutenedial) to $p(\text{RO}_x)$ decreased at both sites. The impact of the new photolysis mechanism was more pronounced at the PRD regional site, likely due to the higher fractions of OVOCs in downwind areas (Liang et al., 2022).

As radical production is increased using the new photolysis mechanism, ozone production is also enhanced. The enhancement of ozone production rate $p(\text{O}_3)$ at noon was relatively modest, with increases of 5.3% at the urban site and 3.9% at the regional site. Similarly, peroxyacetyl nitrate (PAN), a typical photochemical product, exhibited minor sensitivity to the new mechanism, with noon concentrations increasing by 2.2%–6.9% at both sites. This may result from modifications to the photolysis rate constants of a wide range of OVOCs in the new mechanism, where the opposing effects of increased and decreased rates effectively counter-balanced each other, masking the impact of OVOC photolysis on secondary species formation.

3.3 Identifying key non-HCHO species contributing to $p(\text{RO}_x)$

Only HCHO concentrations were constrained in Scenario 1 of model simulation, which may bear substantial biases

within simulated concentrations of other photodegradable OVOCs and hence influence identification of key species that significantly contribute to $p(\text{RO}_x)$. For example, the new mechanism incorporated the photolysis of nitrophenol, partially alleviating its overestimation, yet the simulated concentrations remained significantly higher than observations (see Fig. S7). This residual overestimation may be attributed to enhanced secondary formation driven by accelerated RO_x cycling, as well as the absence of heterogeneous loss processes such as particle-phase reactions and deposition. To identify key species among numerous photodegradable OVOCs, Scenario 2 imposes extensive constraints on intermediate products to approximate a “quasi-realistic” VOC composition. Under these conditions, the impacts of the new photolysis mechanism on $p(\text{RO}_x)$ are investigated across three different environments. OVOCs contributed over 50% of VOCs at all sites, with the highest OVOC contribution at the PRD regional site (56%).

After constraining intermediate species in the model, non-HCHO OVOCs still show a significant contribution to $p(\text{RO}_x)$. At the urban sites, non-HCHO OVOCs contributed 27% (Guangzhou) and 25% (Beijing) to $p(\text{RO}_x)$, while at the PRD regional site, this contribution was higher at 45%, with an average $p(\text{RO}_x)$ of 16 ppb d^{-1} (Fig. 9a, c, e). Despite similar j_{NO_2} values at the PRD regional site and the Guangzhou urban site (Fig. S8), the PRD regional site showed a significantly higher $p(\text{RO}_x)$, indicating that higher OVOC concentrations and more aged air masses are key drivers of radical production in the regional environment. This contrast suggests that under these conditions, the composition and concentration of OVOCs play a more crucial role in radical production than photolysis intensity.

Further analysis of the relative fractions reveals regional differences in the contribution of non-HCHO OVOC photolysis to $p(\text{RO}_x)$ throughout the day. At the PRD regional site, the contribution of non-HCHO OVOC increased with solar radiation, peaking at 46% at noon and then stabilizing before declining after sunset (Fig. 9d). This peak corresponds to maximum radiation, and the afternoon stability suggests replenishment by the oxidation of transported VOCs from upwind megacities. In contrast, the contribution at both urban sites peaked at 35% at 07:00 LT and then gradually declined to 25%–30% before sharply dropping prior to sunset (Fig. 9b, f). The morning peak is likely due to primary emissions or photolysis of overnight-accumulated OVOCs, while lower daytime values reflect limited photodegradable OVOCs in fresher air. In summary, the contribution of non-HCHO OVOC photolysis to $p(\text{RO}_x)$ exhibited a unimodal diurnal pattern at the PRD regional site, while a morning peak was observed at both urban sites.

An analysis of the contribution of non-HCHO OVOC photolysis to $p(\text{RO}_x)$ was conducted based on the structure of OVOCs (Fig. 10a, c, e). Both urban sites exhibited similar trends, with OVOCs containing a single carbonyl group dominating their contribution to $p(\text{RO}_x)$. At the

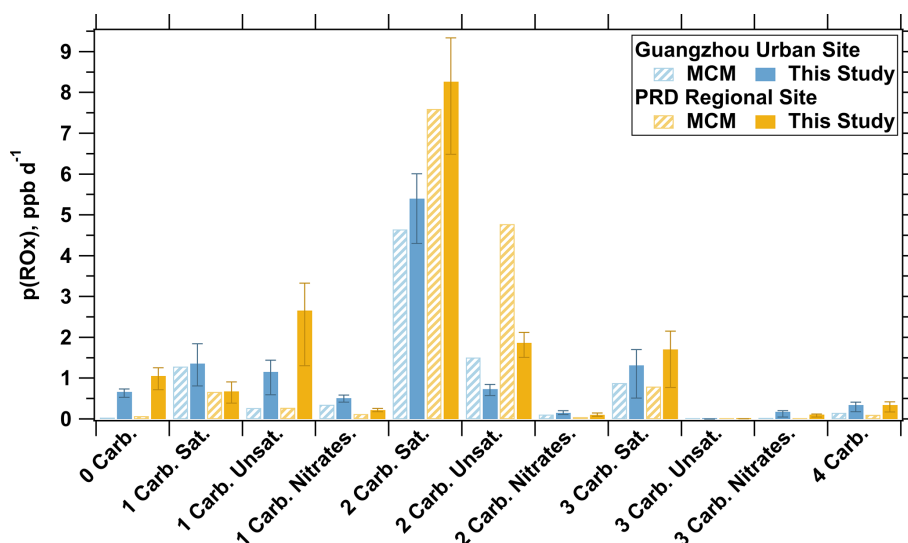


Figure 8. Comparison of the contributions of different OVOC types to total $p(\text{RO}_x)$ at urban and regional sites under Scenario 1. Blue bars represent the urban site, while yellow bars represent the regional site. Error bars (this study only) show the range from using the maximum and minimum estimated photolysis rate constants in the simulations.

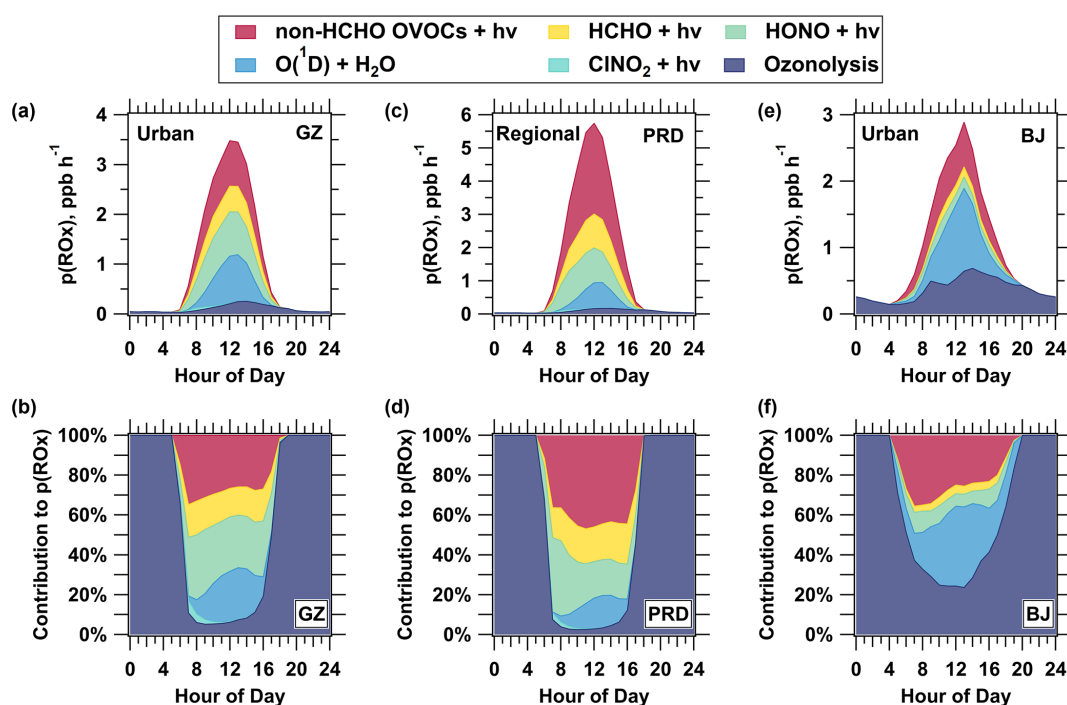


Figure 9. Source composition and pathway contributions of total $p(\text{RO}_x)$ at three sites under Scenario 2. The first row (a, c, e) represents the $p(\text{RO}_x)$ source composition at the Guangzhou urban site (GZ, a), PRD regional site (PRD, c), and Beijing urban site (BJ, e). The second row (b, d, f) shows the contributions of different pathways to $p(\text{RO}_x)$ at the corresponding sites.

Beijing urban site, these mono-carbonyl OVOCs accounted for nearly half of the non-HCHO OVOCs, most of which were saturated compounds. Mono-carbonyls contributed approximately 13% to the total $p(\text{RO}_x)$ at the Guangzhou urban site and 14% at the Beijing urban site, given that non-

HCHO OVOCs contributed around 27% and 25%, respectively. Di-carbonyl OVOCs contributed second-most at both urban sites, mostly from saturated compounds, while compounds with 3 to 5 carbonyl groups contributed 9%–12%. In contrast, di-carbonyl compounds were the primary con-

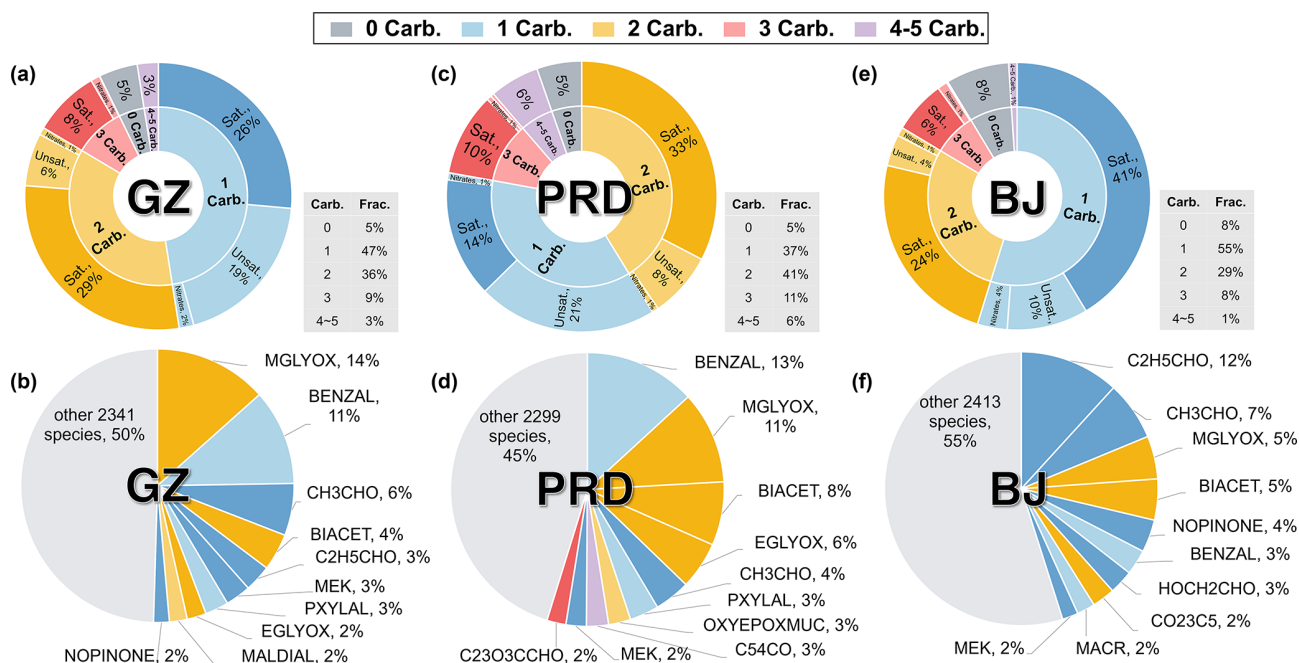


Figure 10. Contribution of OVOCs with different carbonyl counts to $p(\text{RO}_x)$ and the top 10 contributing species in Scenario 2. The first row (a, c, e) shows the fraction of OVOCs with different numbers of carbonyl groups, where Sat. stands for saturated, Unsat. for unsaturated, and Nitrates for organic nitrates. Similar colors indicate species with the same number of carbonyl groups. The gray table at the bottom right of the sunburst chart displays the total fraction for each category of carbonyl groups. The second row (b, d, f) presents the MCM names and specific contributions of the top 10 contributing species. Results for the Guangzhou urban site are shown in (a, b), for the PRD regional site in (c, d), and for the Beijing urban site in (e, f).

tributor at the PRD regional site, with an increased contribution of unsaturated mono-carbonyls. Compounds with 3 to 5 carbonyl groups contributed 17% at the PRD regional site, significantly higher than at urban sites, highlighting the role of more oxidized and multifunctional species in regional environments. Compounds without carbonyl groups, such as nitrophenol and organic nitrates, contributed minimally (5%–8%) across all sites, likely due to lower concentrations or slower photolysis rates. Generally, mono-carbonyl OVOCs dominate $p(\text{RO}_x)$ at urban sites, while multiple carbonyl OVOCs are more important at the regional site.

From an individual species perspective, the top 10 non-HCHO OVOCs accounted for more than half of the total non-HCHO OVOC contribution to $p(\text{RO}_x)$ at all sites (Fig. 10b, d, f). At urban sites, the contributions are primarily driven by OVOCs containing 1–2 carbonyl groups, contributing 50% at the Guangzhou urban site and 45% at the Beijing urban site. At the PRD regional site, contributions from di-carbonyl and multi-carbonyl (3–4 carbonyl groups) compounds increased significantly. The top 10 non-HCHO OVOCs across all sites mainly included oxidation products from alkenes, ring-retaining products, and multi-carbonyl ring-opening products from aromatic oxidation, as well as aldehydes. Notably, biogenic VOC oxidation products such as those from isoprene and β -pinene (e.g., nopinone) were prominent at both urban sites, highlighting the potential im-

portance of biogenic VOCs in OVOC formation in urban areas. Although the individual contributions of the remaining OVOCs (over 2000 species) outside the top 10 were small, their cumulative impact remained notable.

4 Conclusion

In this study, a structure-based parameterization for OVOC photolysis rate constants has been developed, together with an OVOC photolysis mechanism supplementary module based on the MCM v3.3.1 mechanism. The proposed method effectively reproduces photolysis rate constants for 104 compounds using 21 reference values and 10 adjustment coefficients. Additionally, it identifies 714 photodegradable species not considered photolyzable in MCM v3.3.1. The integration of the new photolysis mechanism leads to a 13% increase in $p(\text{RO}_x)$ at both the Guangzhou urban site and PRD regional site, contributing 27% and 56% to daily $p(\text{RO}_x)$, respectively. For multi-carbonyl compounds, photolysis contributes more to their atmospheric removal than reactions with OH radicals. After innovatively using the model results to allocate mass spectrometry data and constrain more intermediate species, the model still reveals significant contributions of non-HCHO OVOC photolysis to $p(\text{RO}_x)$. Non-HCHO OVOC photolysis contributes 25%–27% to $p(\text{RO}_x)$ at both urban sites and 45% at the PRD

regional site, surpassing the contribution of HCHO photolysis. The diurnal variations in the fraction of $p(\text{RO}_x)$ contributed by non-HCHO OVOC photolysis highlight the importance of primary OVOC emissions at urban sites and the oxidation of transported VOCs at the PRD regional site. The top 10 species contribute over half of the non-HCHO OVOC contribution to $p(\text{RO}_x)$, while the remaining more than 2000 species collectively make a noteworthy contribution. Photolysis of multifunctional compounds produced from the oxidation of alkenes and aromatics plays a major role in radical production.

By establishing a relationship between species structure and photolysis frequencies, this study circumvents the limitation of insufficient quantum yield data, enabling the derivation of photolysis mechanisms for compounds whose photolysis frequencies have not been previously measured. The estimated rate constants, combined with species concentrations from model simulations, allow for the identification of key species that significantly contribute to radical production in different environments. This approach not only provides a species-specific evaluation of OVOC photolysis but also offers valuable insights for future laboratory experiments, field observations, and the optimization of chemical mechanisms. Nevertheless, some species remain insufficiently characterized in terms of their photolysis rate constants or mechanisms. For example, the photolysis rate constant of nitrophenol varies notably among different studies. The photolysis behavior of pinene oxidation products has been scarcely examined (Wang et al., 2023), and in this study, their mechanisms were surrogated by using those of cyclo-ketones. Additionally, several compounds with strong photolysis potential, such as alkyl nitrites and N-nitrosamines, are not yet included in the MCM mechanism and require further investigation. Research on multifunctional OVOCs, particularly multi-carbonyl compounds, is still limited. Future experimental efforts are expected to generate more comprehensive data, thereby refining the existing OVOC photolysis mechanisms and ultimately enhancing our understanding of atmospheric chemistry.

Code and data availability. The observational data and parameterization tool kit used in this study are available from corresponding authors upon request (byuan@jnu.edu.cn). The new mechanisms used in this study is available on Figshare: <https://doi.org/10.6084/m9.figshare.28743071> (Peng, 2025).

Supplement. The supplement related to this article is available online at <https://doi.org/10.5194/acp-25-7037-2025-supplement>.

Author contributions. YP, BY, and MS designed the research. SW, XS, WW, SY, JQ, XH, YH, and XBL contributed to the field campaign and data collection. YP performed the data analysis and

parameterization of photolysis data. YP, BY, and MS prepared the manuscript. All the authors reviewed the manuscript.

Competing interests. The contact author has declared that none of the authors has any competing interests.

Disclaimer. Publisher's note: Copernicus Publications remains neutral with regard to jurisdictional claims made in the text, published maps, institutional affiliations, or any other geographical representation in this paper. While Copernicus Publications makes every effort to include appropriate place names, the final responsibility lies with the authors.

Acknowledgements. We gratefully acknowledge the additional support provided by the crews of the three field campaigns.

Financial support. This work was supported by the National Natural Science Foundation of China (grant nos. 42275103 and 42121004) and National Key Research and Development Program of China (grant no. 2023YFC3706200).

Review statement. This paper was edited by Kelvin Bates and reviewed by two anonymous referees.

References

- Aumont, B., Szopa, S., and Madronich, S.: Modelling the evolution of organic carbon during its gas-phase tropospheric oxidation: development of an explicit model based on a self-generating approach, *Atmos. Chem. Phys.*, 5, 2497–2517, <https://doi.org/10.5194/acp-5-2497-2005>, 2005.
- Bloss, C., Wagner, V., Jenkin, M. E., Volkamer, R., Bloss, W. J., Lee, J. D., Heard, D. E., Wirtz, K., Martin-Reviejo, M., Rea, G., Wenger, J. C., and Pilling, M. J.: Development of a detailed chemical mechanism (MCMv3.1) for the atmospheric oxidation of aromatic hydrocarbons, *Atmos. Chem. Phys.*, 5, 641–664, <https://doi.org/10.5194/acp-5-641-2005>, 2005.
- Cai, M., Ye, C., Yuan, B., Huang, S., Zheng, E., Yang, S., Wang, Z., Lin, Y., Li, T., Hu, W., Chen, W., Song, Q., Li, W., Peng, Y., Liang, B., Sun, Q., Zhao, J., Chen, D., Sun, J., Yang, Z., and Shao, M.: Enhanced daytime secondary aerosol formation driven by gas–particle partitioning in downwind urban plumes, *Atmos. Chem. Phys.*, 24, 13065–13079, <https://doi.org/10.5194/acp-24-13065-2024>, 2024.
- Calvert, J. G., Atkinson, R., Becker, K. H., Kamens, R. M., Seinfeld, J. H., Wallington, T. H., and Yarwood, G.: Primary photochemical processes of the aromatic hydrocarbons and some of their common oxidation products, in: *The Mechanisms of Atmospheric Oxidation of the Aromatic Hydrocarbons*, Oxford University Press, 230–310, ISBN 0-19-514628-X, 2002.
- Calvert, J. G., Mellouki, A., Orlando, J. J., Pilling, M. J., and Wallington, T. J.: *Mechanisms of Photodecomposition of the*

- Sunlight-Absorbing Oxygenates, in: *Mechanisms of Atmospheric Oxidation of the Oxygenates*, Oxford University Press, 974–1357, ISBN 978-0-19-976707-6, 2011.
- Carter, W. P. L., Jiang, J., Orlando, J. J., and Barsanti, K. C.: Derivation of atmospheric reaction mechanisms for volatile organic compounds by the SAPRC mechanism generation system (MechGen), *Atmos. Chem. Phys.*, 25, 199–242, <https://doi.org/10.5194/acp-25-199-2025>, 2025.
- Chen, Y., Zheng, P., Wang, Z., Pu, W., Tan, Y., Yu, C., Xia, M., Wang, W., Guo, J., Huang, D., Yan, C., Nie, W., Ling, Z., Chen, Q., Lee, S., and Wang, T.: Secondary Formation and Impacts of Gaseous Nitro-Phenolic Compounds in the Continental Outflow Observed at a Background Site in South China, *Environ. Sci. Technol.*, 56, 6933–6943, <https://doi.org/10.1021/acs.est.1c04596>, 2022.
- Edwards, P. M., Brown, S. S., Roberts, J. M., Ahmadov, R., Banta, R. M., deGouw, J. A., Dube, W. P., Field, R. A., Flynn, J. H., Gilman, J. B., Graus, M., Helmig, D., Koss, A., Langford, A. O., Lefer, B. L., Lerner, B. M., Li, R., Li, S. M., McKeen, S. A., Murphy, S. M., Parrish, D. D., Senff, C. J., Soltis, J., Stutz, J., Sweeney, C., Thompson, C. R., Trainer, M. K., Tsai, C., Veres, P. R., Washenfelder, R. A., Warneke, C., Wild, R. J., Young, C. J., Yuan, B., and Zamora, R.: High winter ozone pollution from carbonyl photolysis in an oil and gas basin, *Nature*, 514, 351–354, <https://doi.org/10.1038/nature13767>, 2014.
- Eger, P. G., Schuladen, J., Sobanski, N., Fischer, H., Karu, E., Williams, J., Riva, M., Zha, Q., Ehn, M., Quéléver, L. L. J., Schallhart, S., Lelieveld, J., and Crowley, J. N.: Pyruvic acid in the boreal forest: gas-phase mixing ratios and impact on radical chemistry, *Atmos. Chem. Phys.*, 20, 3697–3711, <https://doi.org/10.5194/acp-20-3697-2020>, 2020.
- Griffith, S. M., Hansen, R., Dusanter, S., Michoud, V., Gilman, J., Kuster, W., Veres, P., Graus, M., de Gouw, J., and Roberts, J.: Measurements of hydroxyl and hydroperoxy radicals during CalNex-LA: Model comparisons and radical budgets, *J. Geophys. Res.-Atmos.*, 121, 4211–4232, <https://doi.org/10.1002/2015JD024358>, 2016.
- He, X., Yuan, B., Wu, C., Wang, S., Wang, C., Huangfu, Y., Qi, J., Ma, N., Xu, W., Wang, M., Chen, W., Su, H., Cheng, Y., and Shao, M.: Volatile organic compounds in wintertime North China Plain: Insights from measurements of proton transfer reaction time-of-flight mass spectrometer (PTR-ToF-MS), *J. Environ. Sci.*, 114, 98–114, <https://doi.org/10.1016/j.jes.2021.08.010>, 2022.
- Huang, X.-F., Zhang, B., Xia, S.-Y., Han, Y., Wang, C., Yu, G.-H., and Feng, N.: Sources of oxygenated volatile organic compounds (OVOCs) in urban atmospheres in North and South China, *Environ. Pollut.*, 261, 114152, <https://doi.org/10.1016/j.envpol.2020.114152>, 2020.
- Huangfu, Y., Yuan, B., He, X., Liu, Z., Zhang, Y., Karl, T., Striednig, M., Ding, Y., Chen, X., and Li, H.: Natural Gas Leakage Ratio Determined from Flux Measurements of Methane in Urban Beijing, *Environ. Sci. Technol. Lett.*, 11, 1025–1031, <https://doi.org/10.1021/acs.estlett.4c00573>, 2024.
- Hui, L., Liu, X., Tan, Q., Feng, M., An, J., Qu, Y., Zhang, Y., and Jiang, M.: Characteristics, source apportionment and contribution of VOCs to ozone formation in Wuhan, Central China, *Atmos. Environ.*, 192, 55–71, <https://doi.org/10.1016/j.atmosenv.2018.08.042>, 2018.
- IUPAC: IUPAC Task Group on Atmospheric Chemical Kinetic Data Evaluation, International Union of Pure and Applied Chemistry [data set], <https://iupac.aeris-data.fr/> (last access: 2 March 2025), 2012.
- Jenkin, M. E., Saunders, S. M., and Pilling, M. J.: The tropospheric degradation of volatile organic compounds: a protocol for mechanism development, *Atmos. Environ.*, 31, 81–104, [https://doi.org/10.1016/S1352-2310\(96\)00105-7](https://doi.org/10.1016/S1352-2310(96)00105-7), 1997.
- Jenkin, M. E., Saunders, S. M., Wagner, V., and Pilling, M. J.: Protocol for the development of the Master Chemical Mechanism, MCM v3 (Part B): tropospheric degradation of aromatic volatile organic compounds, *Atmos. Chem. Phys.*, 3, 181–193, <https://doi.org/10.5194/acp-3-181-2003>, 2003.
- Jenkin, M. E., Young, J. C., and Rickard, A. R.: The MCM v3.3.1 degradation scheme for isoprene, *Atmos. Chem. Phys.*, 15, 11433–11459, <https://doi.org/10.5194/acp-15-11433-2015>, 2015.
- Jing, S.-A., Gao, Y.-Q., Shen, J.-D., Wang, Q., Peng, Y.-R., Li, Y.-J., and Wang, H.-L.: Characteristics and reactivity of ambient VOCs in urban Hangzhou, China, *Environ. Sci.*, 41, 5306–5315, <https://doi.org/10.13227/j.hjhx.202004021>, 2020.
- Kanaya, Y., Cao, R., Akimoto, H., Fukuda, M., Komazaki, Y., Yokouchi, Y., Koike, M., Tanimoto, H., Takegawa, N., and Kondo, Y.: Urban photochemistry in central Tokyo: 1. Observed and modeled OH and HO₂ radical concentrations during the winter and summer of 2004, *J. Geophys. Res.-Atmos.*, 112, D21, <https://doi.org/10.1029/2007JD008670>, 2007.
- Keller-Rudek, H., Moortgat, G. K., Sander, R., and Sørensen, R.: The MPI-Mainz UV/VIS Spectral Atlas of Gaseous Molecules of Atmospheric Interest, *Earth Syst. Sci. Data*, 5, 365–373, <https://doi.org/10.5194/essd-5-365-2013>, 2013.
- Kroll, J. H., Donahue, N. M., Jimenez, J. L., Kessler, S. H., Canagaratna, M. R., Wilson, K. R., Altieri, K. E., Mazzoleni, L. R., Wozniak, A. S., Bluhm, H., Mysak, E. R., Smith, J. D., Kolb, C. E., and Worsnop, D. R.: Carbon oxidation state as a metric for describing the chemistry of atmospheric organic aerosol, *Nature Chem.*, 3, 133–139, <https://doi.org/10.1038/nchem.948>, 2011.
- Lantz, K. O., Shetter, R. E., Cantrell, C. A., Flocke, S. J., Calvert, J. G., and Madronich, S.: Theoretical, actinometric, and radiometric determinations of the photolysis rate coefficient of NO₂ during the Mauna Loa Observatory Photochemistry Experiment 2, *J. Geophys. Res.-Atmos.*, 101, 14613–14630, <https://doi.org/10.1029/96JD00215>, 1996.
- Li, K., Jacob, D. J., Liao, H., Qiu, Y., Shen, L., Zhai, S., Bates, K. H., Sulprizio, M. P., Song, S., and Lu, X.: Ozone pollution in the North China Plain spreading into the late-winter haze season, *P. Natl. Acad. Sci. USA*, 118, e2015797118, <https://doi.org/10.1073/pnas.2015797118>, 2021.
- Li, X.-B., Yuan, B., Huangfu, Y., Yang, S., Song, X., Qi, J., He, X., Wang, S., Chen, Y., Yang, Q., Song, Y., Peng, Y., Tang, G., Gao, J., Gu, D., and Shao, M.: Vertical changes in volatile organic compounds (VOCs) and impacts on photochemical ozone formation, *Atmos. Chem. Phys.*, 25, 2459–2472, <https://doi.org/10.5194/acp-25-2459-2025>, 2025.
- Li, Y., Yin, S., Yu, S., Yuan, M., Dong, Z., Zhang, D., Yang, L., and Zhang, R.: Characteristics, source apportionment and health risks of ambient VOCs during high ozone period at an urban site in central plain, China, *Chemosphere*, 250, 126283, <https://doi.org/10.1016/j.chemosphere.2020.126283>, 2020.

- Liang, Y., Weber, R. J., Misztal, P. K., Jen, C. N., and Goldstein, A. H.: Aging of volatile organic compounds in October 2017 northern California wildfire plumes, *Environ. Sci. Technol.*, 56, 1557–1567, <https://doi.org/10.1021/acs.est.1c05684>, 2022.
- Liu, Y., Song, M., Liu, X., Zhang, Y., Hui, L., Kong, L., Zhang, Y., Zhang, C., Qu, Y., and An, J.: Characterization and sources of volatile organic compounds (VOCs) and their related changes during ozone pollution days in 2016 in Beijing, China, *Environ. Pollut.*, 257, 113599, <https://doi.org/10.1016/j.envpol.2019.113599>, 2020.
- Liu, Z., Wang, Y., Gu, D., Zhao, C., Huey, L. G., Stickel, R., Liao, J., Shao, M., Zhu, T., Zeng, L., Amoroso, A., Costabile, F., Chang, C.-C., and Liu, S.-C.: Summertime photochemistry during CAREBeijing-2007: RO_x budgets and O₃ formation, *Atmos. Chem. Phys.*, 12, 7737–7752, <https://doi.org/10.5194/acp-12-7737-2012>, 2012.
- Liu, Z., Nguyen, V. S., Harvey, J., Müller, J.-F., and Peeters, J.: The photolysis of α -hydroperoxycarbonyls, *Phys. Chem. Chem. Phys.*, 20, 6970–6979, <https://doi.org/10.1039/c7cp08421h>, 2018.
- Madronich, S. and Flocke, S.: The role of solar radiation in atmospheric chemistry, in: *Environmental Photochemistry*, 1 ed., edited by: Boule, P., Springer Berlin, Heidelberg, 1–26, https://doi.org/10.1007/978-3-540-69044-3_1, 1999.
- McDonald, B. C., De Gouw, J. A., Gilman, J. B., Jathar, S. H., Akherati, A., Cappa, C. D., Jimenez, J. L., Lee-Taylor, J., Hayes, P. L., and McKeen, S. A.: Volatile chemical products emerging as largest petrochemical source of urban organic emissions, *Science*, 359, 760–764, <https://doi.org/10.1126/science.aaq0524>, 2018.
- Mellouki, A., Wallington, T., and Chen, J.: Atmospheric chemistry of oxygenated volatile organic compounds: impacts on air quality and climate, *Chem. Rev.*, 115, 3984–4014, <https://doi.org/10.1021/cr500549n>, 2015.
- Mellouki, A., Ammann, M., Cox, R. A., Crowley, J. N., Herrmann, H., Jenkin, M. E., McNeill, V. F., Troe, J., and Wallington, T. J.: Evaluated kinetic and photochemical data for atmospheric chemistry: volume VIII – gas-phase reactions of organic species with four, or more, carbon atoms ($\geq C_4$), *Atmos. Chem. Phys.*, 21, 4797–4808, <https://doi.org/10.5194/acp-21-4797-2021>, 2021.
- Müller, J.-F., Peeters, J., and Stavrakou, T.: Fast photolysis of carbonyl nitrates from isoprene, *Atmos. Chem. Phys.*, 14, 2497–2508, <https://doi.org/10.5194/acp-14-2497-2014>, 2014.
- Newland, M. J., Rea, G. J., Thuner, L. P., Henderson, A. P., Golding, B. T., Rickard, A. R., Barnes, I., and Wenger, J.: Photochemistry of 2-butenedial and 4-oxo-2-pentenal under atmospheric boundary layer conditions, *Phys. Chem. Chem. Phys.*, 21, 1160–1171, <https://doi.org/10.1039/c8cp06437g>, 2019.
- Peng, Y.: MCMv331_OVOCshv_updated_Mech, figshare [code], <https://doi.org/10.6084/m9.figshare.28743071> (last access: April 2025), 2025.
- Peng, Y. W., Yuan, B., Yang, S. X., Wang, S. H., Yang, X. Y., Wang, W. J., Li, J., Song, X., Wu, C. H., Qi, J. P., Zheng, E., Ye, C. S., Huang, S., Hu, W. W., Song, W., Wang, X. M., Wang, B. L., and Shao, M.: Photolysis frequency of nitrophenols derived from ambient measurements, *Sci. Total Environ.*, 869, 161810, <https://doi.org/10.1016/j.scitotenv.2023.161810>, 2023.
- Qu, H., Wang, Y., Zhang, R., Liu, X., Huey, L. G., Sjostedt, S., Zeng, L., Lu, K., Wu, Y., and Shao, M.: Chemical production of oxygenated volatile organic compounds strongly enhances boundary-layer oxidation chemistry and ozone production, *Environ. Sci. Technol.*, 55, 13718–13727, <https://doi.org/10.1021/acs.est.1c04489>, 2021.
- Riedel, T. P., Wolfe, G. M., Danas, K. T., Gilman, J. B., Kuster, W. C., Bon, D. M., Vlasenko, A., Li, S.-M., Williams, E. J., Lerner, B. M., Veres, P. R., Roberts, J. M., Holloway, J. S., Lefer, B., Brown, S. S., and Thornton, J. A.: An MCM modeling study of nitril chloride (ClNO₂) impacts on oxidation, ozone production and nitrogen oxide partitioning in polluted continental outflow, *Atmos. Chem. Phys.*, 14, 3789–3800, <https://doi.org/10.5194/acp-14-3789-2014>, 2014.
- Roman, C., Arsene, C., Bejan, I. G., and Olariu, R. I.: Investigations into the gas-phase photolysis and OH radical kinetics of nitrocatechols: implications of intramolecular interactions on their atmospheric behaviour, *Atmos. Chem. Phys.*, 22, 2203–2219, <https://doi.org/10.5194/acp-22-2203-2022>, 2022.
- Song, X., Bin, Y., Si-hang, W., Xian-jun, H., Xiao-bing, L., Yuwen, P., Yu-bin, C., Ji-peng, Q., Jia-hua, C., Shan, H., dan, H., Wen, W., Ke-xuan, L., and Min, S.: Compositional Characteristics of Volatile Organic Compounds in Typical Industrial Areas of the Pearl River Delta: Importance of Oxygenated Volatile Organic Compounds, *Environ. Sci.*, 44, 1336–1345, <https://doi.org/10.13227/j.hjxk.202204104>, 2023.
- Tadić, J., Juranić, I., and Moortgat, G. K.: Pressure dependence of the photooxidation of selected carbonyl compounds in air: n-butanal and n-pentanal, *J. Photochem. Photobiol. A*, 143, 169–179, [https://doi.org/10.1016/S1010-6030\(01\)00524-X](https://doi.org/10.1016/S1010-6030(01)00524-X), 2001.
- Tan, Z., Lu, K., Hofzumahaus, A., Fuchs, H., Bohn, B., Holland, F., Liu, Y., Rohrer, F., Shao, M., Sun, K., Wu, Y., Zeng, L., Zhang, Y., Zou, Q., Kiendler-Scharr, A., Wahner, A., and Zhang, Y.: Experimental budgets of OH, HO₂, and RO₂ radicals and implications for ozone formation in the Pearl River Delta in China 2014, *Atmos. Chem. Phys.*, 19, 7129–7150, <https://doi.org/10.5194/acp-19-7129-2019>, 2019a.
- Tan, Z., Lu, K., Jiang, M., Su, R., Wang, H., Lou, S., Fu, Q., Zhai, C., Tan, Q., Yue, D., Chen, D., Wang, Z., Xie, S., Zeng, L., and Zhang, Y.: Daytime atmospheric oxidation capacity in four Chinese megacities during the photochemically polluted season: a case study based on box model simulation, *Atmos. Chem. Phys.*, 19, 3493–3513, <https://doi.org/10.5194/acp-19-3493-2019>, 2019b.
- Tomas, A., Aslan, L., Muñoz, A., Ródenas, M., Vera, T., Borrás, E., Coddeville, P., and Fittschen, C.: Photolysis of multifunctional carbonyl compounds under natural irradiation at EUPHORE, *Atmos. Environ.*, 253, 118352, <https://doi.org/10.1016/j.atmosenv.2021.118352>, 2021.
- Treves, K. and Rudich, Y.: The Atmospheric Fate of C₃–C₆ Hydroxyalkyl Nitrates, *J. Phys. Chem. A*, 107, 7809–7817, 2003.
- Wang, C., Yuan, B., Wu, C., Wang, S., Qi, J., Wang, B., Wang, Z., Hu, W., Chen, W., Ye, C., Wang, W., Sun, Y., Wang, C., Huang, S., Song, W., Wang, X., Yang, S., Zhang, S., Xu, W., Ma, N., Zhang, Z., Jiang, B., Su, H., Cheng, Y., Wang, X., and Shao, M.: Measurements of higher alkanes using NO⁺ chemical ionization in PTR-ToF-MS: important contributions of higher alkanes to secondary organic aerosols in China, *Atmos. Chem. Phys.*, 20, 14123–14138, <https://doi.org/10.5194/acp-20-14123-2020>, 2020.

- Wang, S., Fan, B., and Dong, X.: Introduction to specification of SMILES and review of its effect of chemical toxicity prediction, *Occupational Health And Emergency Rescue*, 36, 471, <https://doi.org/10.16369/j.oher.issn.1007-1326.2018.05.028>, 2018.
- Wang, W., Yuan, B., Peng, Y., Su, H., Cheng, Y., Yang, S., Wu, C., Qi, J., Bao, F., Huangfu, Y., Wang, C., Ye, C., Wang, Z., Wang, B., Wang, X., Song, W., Hu, W., Cheng, P., Zhu, M., Zheng, J., and Shao, M.: Direct observations indicate photodegradable oxygenated volatile organic compounds (OVOCs) as larger contributors to radicals and ozone production in the atmosphere, *Atmos. Chem. Phys.*, 22, 4117–4128, <https://doi.org/10.5194/acp-22-4117-2022>, 2022.
- Wang, Y., Takeuchi, M., Wang, S., Nizkorodov, S. A., France, S., Eris, G., and Ng, N. L.: Photolysis of gas-phase atmospherically relevant monoterpene-derived organic nitrates, *J. Phys. Chem. A*, 127, 987–999, <https://doi.org/10.1021/acs.jpca.2c04307>, 2023.
- Weininger, D.: SMILES, a chemical language and information system. 1. Introduction to methodology and encoding rules, *J. Chem. Inf. Comput. Sci.*, 28, 31–36, <https://doi.org/10.1021/ci00057a005>, 1988.
- Wolfe, G. M., Marvin, M. R., Roberts, S. J., Travis, K. R., and Liao, J.: The Framework for 0-D Atmospheric Modeling (F0AM) v3.1, *Geosci. Model Dev.*, 9, 3309–3319, <https://doi.org/10.5194/gmd-9-3309-2016>, 2016.
- Wu, C., Wang, C., Wang, S., Wang, W., Yuan, B., Qi, J., Wang, B., Wang, H., Wang, C., Song, W., Wang, X., Hu, W., Lou, S., Ye, C., Peng, Y., Wang, Z., Huangfu, Y., Xie, Y., Zhu, M., Zheng, J., Wang, X., Jiang, B., Zhang, Z., and Shao, M.: Measurement report: Important contributions of oxygenated compounds to emissions and chemistry of volatile organic compounds in urban air, *Atmos. Chem. Phys.*, 20, 14769–14785, <https://doi.org/10.5194/acp-20-14769-2020>, 2020.
- Yang, Q., Li, X.-B., Yuan, B., Zhang, X., Huangfu, Y., Yang, L., He, X., Qi, J., and Shao, M.: Measurement report: Enhanced photochemical formation of formic and isocyanic acids in urban regions aloft – insights from tower-based online gradient measurements, *Atmos. Chem. Phys.*, 24, 6865–6882, <https://doi.org/10.5194/acp-24-6865-2024>, 2024.
- Yang, S., Yuan, B., Peng, Y., Huang, S., Chen, W., Hu, W., Pei, C., Zhou, J., Parrish, D. D., Wang, W., He, X., Cheng, C., Li, X.-B., Yang, X., Song, Y., Wang, H., Qi, J., Wang, B., Wang, C., Wang, C., Wang, Z., Li, T., Zheng, E., Wang, S., Wu, C., Cai, M., Ye, C., Song, W., Cheng, P., Chen, D., Wang, X., Zhang, Z., Wang, X., Zheng, J., and Shao, M.: The formation and mitigation of nitrate pollution: comparison between urban and suburban environments, *Atmos. Chem. Phys.*, 22, 4539–4556, <https://doi.org/10.5194/acp-22-4539-2022>, 2022.
- Yang, X., Xue, L., Wang, T., Wang, X., Gao, J., Lee, S., Blake, D. R., Chai, F., and Wang, W.: Observations and explicit modeling of summertime carbonyl formation in Beijing: identification of key precursor species and their impact on atmospheric oxidation chemistry, *J. Geophys. Res.-Atmos.*, 123, 1426–1440, <https://doi.org/10.1002/2017JD027403>, 2018.
- Ye, C., Yuan, B., Lin, Y., Wang, Z., Hu, W., Li, T., Chen, W., Wu, C., Wang, C., Huang, S., Qi, J., Wang, B., Wang, C., Song, W., Wang, X., Zheng, E., Krechmer, J. E., Ye, P., Zhang, Z., Wang, X., Worsnop, D. R., and Shao, M.: Chemical characterization of oxygenated organic compounds in the gas phase and particle phase using iodide CIMS with FIGAERO in urban air, *Atmos. Chem. Phys.*, 21, 8455–8478, <https://doi.org/10.5194/acp-21-8455-2021>, 2021.
- Young, C. J., Washenfelder, R. A., Roberts, J. M., Mielke, L. H., Osthoff, H. D., Tsai, C., Pikelnaya, O., Stutz, J., Veres, P. R., and Cochran, A. K.: Vertically resolved measurements of nighttime radical reservoirs in Los Angeles and their contribution to the urban radical budget, *Environ. Sci. Technol.*, 46, 10965–10973, <https://doi.org/10.1021/es302206a>, 2012.
- Yuan, B., Liggio, J., Wentzell, J., Li, S.-M., Stark, H., Roberts, J. M., Gilman, J., Lerner, B., Warneke, C., Li, R., Leithead, A., Osthoff, H. D., Wild, R., Brown, S. S., and de Gouw, J. A.: Secondary formation of nitrated phenols: insights from observations during the Uintah Basin Winter Ozone Study (UBWOS) 2014, *Atmos. Chem. Phys.*, 16, 2139–2153, <https://doi.org/10.5194/acp-16-2139-2016>, 2016.
- Yuan, B., Koss, A. R., Warneke, C., Coggon, M., Sekimoto, K., and de Gouw, J. A.: Proton-transfer-reaction mass spectrometry: applications in atmospheric sciences, *Chem. Rev.*, 117, 13187–13229, <https://doi.org/10.1021/acs.chemrev.7b00325>, 2017.